

Local Hydration Control and Functional Implications Through S-Nitrosylation of Proteins: Kirsten rat sarcoma virus (KRAS) and Hemoglobin (Hb)

Haydar Taylan Turan¹ and Markus Meuwly^{1*}

¹*Department of Chemistry, University of Basel, Klingelbergstrasse 80, Basel, Switzerland*

E-mail: m.meuwly@unibas.ch

Abstract

S-nitrosylation, the covalent addition of NO to the thiol side chain of cysteine, is an important post-translational modification (PTM) that can affect the function of proteins. As such, PTMs extend and diversify protein functions and thus characterizing consequences of PTM at a molecular level is of great interest. Although PTMs can be detected through various direct/indirect methods, they lack the capabilities to investigate the modifications at the molecular level. In the present work local and global structural dynamics, their correlation, the hydration structure, and the infrared spectroscopy for WT and S-nitrosylated Kirsten rat sarcoma virus (KRAS) and Hemoglobin (Hb) are characterized from molecular dynamics simulations. It is found that for KRAS attaching NO to Cys118 rigidifies the protein in the Switch-I region which has functional implications, whereas for Hb nitrosylation at Cys93 at the β_1 chain increases the flexibility of secondary structural motives for Hb in its T₀ and R₄ conformational sub-states. Solvent water access decreased by 40% after nitrosylation in KRAS, similar to

Hb for which, however, local hydration of the R₄NO state is yet lower than for T₀NO. Finally, S-nitrosylation leads to detectable peaks for NO stretch, however, congested IR region will make experimental detection of these bands difficult

September 13, 2022

1 Introduction

Post-translational modifications (PTM) comprise covalent modifications of proteins that occur at one or several sites¹ which can lead to structural, local hydration changes and can alter the physio-chemical properties of the proteins and binding partners.² They can impact protein function both allosterically and orthosterically.³ PTMs can be divided into two main groups. The first group classifies the covalent additions of a - usually - electrophilic fragment of a cosubstrate to the side chains of the amino acid⁴ whereas the second group classifies the cleavage of peptide backbones by autocatalytic cleavage or proteases.⁵ Nitrosylation, phosphorylation, oxidation, alkylation, and glycosylation are among the most common types of covalent side-chain modifications.⁴ Backbone PTMs range from methylation of amide nitrogen⁶ to significant alterations to the backbone.⁷

A wide range of experimental techniques has been proposed and applied to detect the PTMs. These methods can be divided into two groups: indirect detection usually breaks the covalent bond between modification and protein and then captures the signals of the PTMs adduct part whereas direct techniques address the adducts directly. Indirect methods such as biotin-switch,⁸ Enzyme-Linked immunosorbent Assay (ELISA)⁹ are robust, but they usually require multi-step sequential manipulation which may hamper the selectivity and reproducibility.¹⁰ Furthermore, they usually only provide whether or not PTM has occurred at a particular site but do not allow for further in-depth physicochemical or structural characterization of the consequences of PTM. Direct methods such as erasable single-molecule

blotting (eSiMBlot) or organophosphine probes are subject to similar selectivity problems as indirect methods as well.¹⁰ Further, spectroscopic techniques can be utilized for the detection of PTM. The mass spectroscopy is one of the widely used techniques for PTM detection.¹¹ Nuclear magnetic resonance (NMR) spectroscopy is used to detect PTM and characterize their effects on protein conformation.¹² Finally, infrared (IR) spectroscopy, is one of the most direct methods as it reports directly on the bond themselves.

The human genome is estimated to comprise $\sim 20,000$ to $25,000$ genes whereas the human proteome is estimated at over 1 million proteins.¹³ The diversity of proteome is provided by two major mechanisms. The first one is mRNA splicing at the transcriptional level, and the second one are PTMs. Hence, PTMs help to extend and diversify proteins function, and in turn the diversity of organism, further than gene transcripts dictate.¹⁴ So, it is important to characterize the effects of PTMs at an atomistic level to have a better understanding about the alteration in protein function induced by modifications ranging from regulation of cell survival,¹⁵ protein aggregation via covalent cross-linking¹⁶ to protein unfolding.¹⁷

Kirsten rat sarcoma virus (KRAS) is one of the three members of the rat sarcome virus (RAS) oncogene family along with the HRAS and NRAS proteins that plays a role in human cancer.¹⁸ Over 20% of human cancers contain mutated RAS genes which makes them the most frequent oncogenic drivers,¹⁹ while KRAS is accounted for 85% of RAS mutations.²⁰ The pancreatic (88%), colorectal (50%) and lung cancers (35%) are types of human cancer with the highest rate of KRAS mutations.²¹ KRAS protein switches between guanosine diphosphate (GDP)-bound inactive state and guanosine triphosphate (GTP)-bound active state. The transformation from a stable GDP-bound state to the active GTP-bound state is stimulated by guanine nucleotide exchange factor (GEF) proteins. The transformation back to the inactive GDP-bound state is mediated by GTPase-activating proteins (GAP). The switch between active and inactive states is highly regulated and responsive to multiple

signal inputs due to the fact that the switch is controlled by GEFs and GAPs.¹⁸

Hemoglobin (Hb) is an important and extensively studied protein due to its role in transporting oxygen from the lungs to the tissues. Deoxy (T_0) and oxy (R_4) structures are two of the most important structural states of the Hb.²² The stability of deoxy and oxy states is subject to the number of ligands bound to the heme-iron. The deoxy state is stable when no ligand is bound to the ferrous iron atom of heme whereas the oxy state is stable when four ligands are bound. Beside oxygen several other ligands such as carbon monoxide (CO), carbon dioxide (CO_2) and nitric oxide (NO) can be bonded to the iron as well. Hb can bind carbon monoxide to the iron and form carboxyhemoglobin which inhibits the oxygen binding due to the occupation of the binding site. Further, binding affinity of hemoglobin is ~ 250 times higher than its affinity for the oxygen.

Protein hydration and protein-water interactions are crucial for chain folding, structure, and conformational stability of proteins.²³ Further, it is known that interactions between proteins and individual water molecules can mediate protein functions such as recognition, binding, or catalysis.²⁴ Although water molecules can also occupy internal cavities and deep clefts, the majority of protein hydration studies focuses on the water interactions with the external surface of the protein.^{25? -27} The water molecule layer which in intimate interaction with a protein surface is called protein hydration shell.²⁸ Local hydration is important in that it can inhibit or promote a PTM by altering solvent and cofactor accessibility around the surrounding region of the modification site. The local hydration of the protein also can be modified by PTM. S-nitrosylation is known to alter the water structure around the cysteine residue.²⁹ Oxidation of Met to the sulfoxide MetSO renders the side chain of Met both, polar and hydrophilic.³⁰ The phosphorylated kinase-induced domain (pKID) showed more hydrophobic interactions after including the modification which promotes the formation of the special hydrophobic residue cluster which includes residues Leu128, Tyr134, Ile137, Leu138, and

Leu141.³¹ Moeller et al. discussed the phosphorylation-dependent regulation of AQP2 water permeability. Also, they state “phosphorylation can change hydrophobic regions of a protein into polar (negatively charged) or hydrophilic”.³² Although the importance of local hydration has been pointed out in the literature, no direct proof of local hydration modification has been reported experimentally.

The present work is structured as follows; First, atomic simulations and methods used in the paper are described. This is followed by the discussion of hydration structure, and local hydrophobicity around the modification site. Then, structural effects and dynamical coupling induced by S-nitrosylation are discussed. Finally, the IR spectra of WT and modified proteins are presented, and conclusions are drawn.

2 Computational Methods

2.1 Molecular Dynamics

All molecular Dynamics (MD) simulations were performed using the CHARMM³³ software with the CHARMM36³⁴ force field. The equations of motion were propagated with a leapfrog integrator,³⁵ using a time step of $\Delta t = 1$ fs and all bonds involving hydrogen atoms were constrained using SHAKE.³⁶ Non-bonded interactions were treated with a switch function³⁷ between 12 and 16 Å and electrostatic interactions were computed with the particle mesh Ewald method.³⁸

For the simulations involving wild-type and S-nitrosylated KRAS, twelve different simulations were set up: wild-type KRAS (PDB: 4OBE)³⁹ at 50 and 300 K, wild-type KRAS without GDP at 50 and 300 K, cis- and trans-S-nitrosylated KRASNO at 50 and 300 K, and cis- and trans-S-nitrosylated KRASNO without GDP at 50 and 300 K. Two chains with identical sequence were available in the crystal structure. Chain A was selected for the sim-

ulation setup. The cis-KRASNO and trans-KRASNO set up starting from the same initial structure except for the dihedral angle $\phi(\text{C}_\beta\text{SNO})$ (0° for cis- and 180° for trans-KRASNO).

For the simulations involving wild-type and S-nitrosylated Hb twenty different simulations were set up: wild-type T_0 Hb (PDB: 2DN2) at 50K and 300 K, wild-type R_4 Hb (PDB: 2DN3) at 50K and 300K, cis- and trans-S-nitrosylated T_0 Hb (T_0NO) at 50 and 300 K with PC and MTP, cis- and trans-S-nitrosylated R_4 Hb (R_4NO) at 50 and 300 K with PC and MTP. cis- and trans- conformers are set up starting from the same initial structure except for the dihedral angle $\phi(\text{C}_\beta\text{SNO})$ (0° for cis- and 180° for trans-KRASNO).

KRAS and Hb were solvated in a $66 \times 66 \times 66 \text{ \AA}^3$ and $90 \times 90 \times 90 \text{ \AA}^3$ cubic boxes of TIP3P⁴⁰ water, respectively. The protein was weakly constrained to the middle of the simulation box, minimized, heated to the desired temperature, and equilibrated for 500 ps in the NVT ensemble. Production runs of 10 ns were then performed in the NpT ensemble using the leapfrog Verlet integrator⁴¹ ($\Delta t = 1 \text{ fs}$) and a Hoover barostat⁴² with a collision rate of 5 ps^{-1} . The force field employed for the -SNO moiety was parameterized as described in the previous study.²⁹

2.2 Infrared Spectroscopy

The molecular dipole moment (μ) of the protein was calculated from the MD trajectories and the partial charges. Subsequently, the Fourier transform of the dipole moment autocorrelation function computed to obtain the infrared spectrum. The autocorrelation function

$$C(t) = \langle \vec{\mu}(0) \cdot \vec{\mu}(t) \rangle \tag{1}$$

was accumulated over 2^{16} time origins to cover 1/3 to 1/2 of the trajectory. From this, the absorption spectrum is determined according to

$$A(\omega) = \omega(1 - e^{-h\omega/(k_B T)}) \int C(t) e^{-i\omega t} dt \quad (2)$$

where T is the temperature in Kelvin, k_B is the Boltzmann constant, and the integral is determined using a fast Fourier transform (FFT). IR spectra of WT KRAS, cis-KRASNO, and trans-KRASNO, WT Hb, cis-T₀NO, trans-T₀NO, cis-R₄NO and trans-R₄NO have been generated for blocks of 100 ps simulation by correlating over 2^{16} time origins. A total of 100 spectra were generated for each system (total simulation time of 10 ns) and averaged.

In addition to IR spectra, the power spectrum of the NO bond was calculated from the FFT of the bond length time-series autocorrelation function to provide assignments of the vibrational spectra and allows to detect couplings between modes.⁴³ These power spectra were not averaged and correlated over 2^{16} time origins for the entire simulation time of 10 ns.

2.3 Dynamical Cross-Correlation Maps

The dynamical cross-correlation maps (DCCM) and difference dynamical cross-correlation maps^{44,45} (Δ DCCM) were calculated to quantitatively characterize the effects of S-nitrosylation on the protein dynamics using the Bio3D package.⁴⁶ Dynamic cross-correlation maps matrices and coefficients

$$C_{ij} = \langle \Delta r_i \cdot \Delta r_j \rangle / (\langle \Delta r_i^2 \rangle \langle \Delta r_j^2 \rangle)^{1/2} \quad (3)$$

were determined from the position of C _{α} in amino acids i and j with positions r_i and r_j . Δr_i and Δr_j determine the displacement of the i th C _{α} from its average position throughout the trajectory. One should note that DCCM characterizes the correlated ($C_{ij} > 0$) and anti-correlated ($C_{ij} < 0$) motions in a protein whereas Δ DCCM reports on the distinct differences

between unmodified and modified protein.

3 Results

The present work reports on the solvation, structural, dynamical and spectroscopic implications of S-nitrosylation at Cys118 for KRAS and at Cys93 β for Hb, see Figure 1.

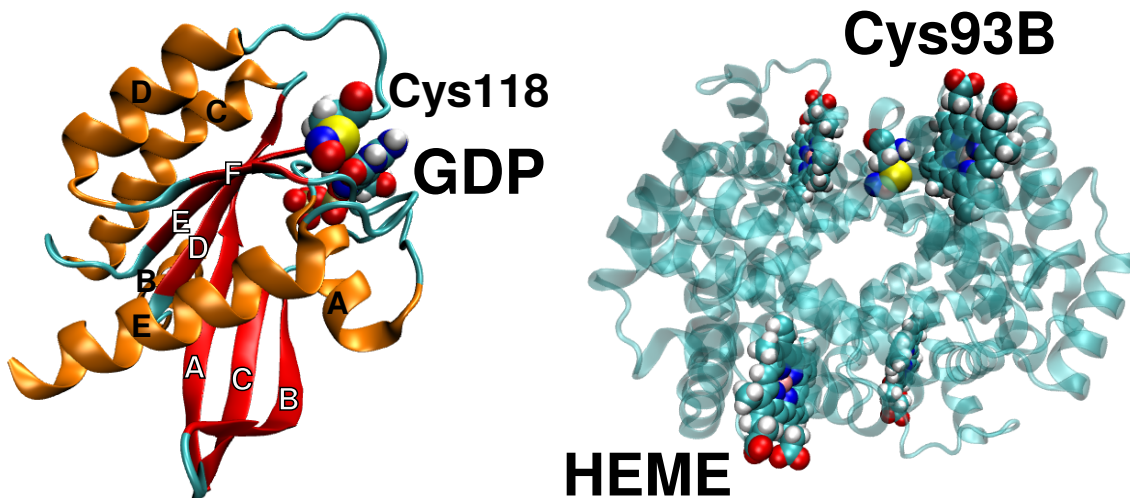


Figure 1: Left: Structure of trans-KRASNO with GDP (PDB: 4OBE). The labeled α -helices are shown in orange, β -sheets are in red and loops are in cyan. Right: Structure of cis-T₀NO (PDB: 2DN2). The S-Nitrosylated Cys118 and Cys93 β residues, GDP and HEME are represented by CPK.

3.1 Local and Global Structural Changes

KRAS: The root-mean-squared fluctuations of the C $_{\alpha}$ atoms of every residue at 300 K from 10 ns simulations with and without GDP are reported in Figure 2 (top and bottom) for WT (black), cis-KRASNO (red), and trans-KRASNO (blue). For simulations with GDP, attaching NO decreased the flexibility of residues Phe28 to Asp33 (Loop B) for cis-KRASNO compared to WT and trans-KRASNO. The importance of this region is arising from the fact the residues are on the Switch-1 region (Phe28 to Asp38). Switch regions act as a binding interface for effector proteins and RAS regulators.⁴⁷ Therefore, rigidification of these

regions potentially affect the binding characteristics of KRAS protein. Moreover, the second switch region (Switch-II, Tyr58 to Tyr64) is also affected by the modification. The modification increased the flexibility of residues Tyr58 to Arg68 in both cis- and trans-KRASNO with respect to WT. The RMSF values increased up to 2.8 Å and 2.5 Å for trans- and cis-KRASNO, respectively, from 1.6 Å for WT. Increased flexibility was also observed for the residues Val103 to Asp108 which are residues on the end of Helix C and the beginning of Loop D. Interestingly, the flexibility of Ser122 was significantly higher in WT compared to nitrosylated variants.

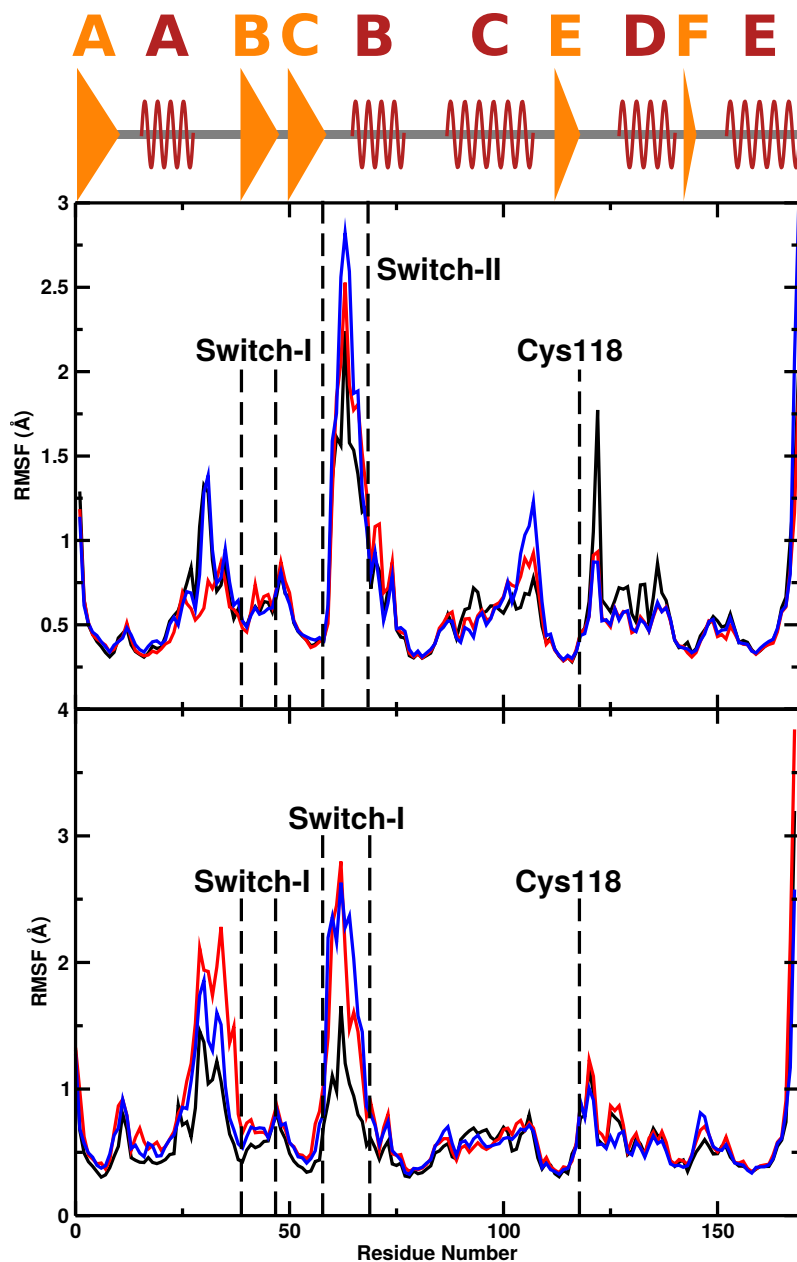


Figure 2: Root Mean Square Fluctuation of each residue at 300 K from simulations with (top) and without GDP (bottom) using the PC model for WT (black), *cis*-KRASNO (red), *trans*-KRASNO (blue). Orange triangles indicate the position of β -sheets and red helices indicate the position of α -helices.

For the simulations without GDP, NO attachment induced increased flexibility of both Switch regions. The RMSF values increased for residues His27 to Ile45, the residues reside on Switch-1 (Loop B) and β -sheet B. However, unlike simulations with GDP, both *cis*- and

trans-KRASNO had increased flexibility in this region compared to WT. The RMSF values increased up to 2.3 and 1.9 Å for cis- and trans-KRASNO, respectively. Further, the flexibility increased also observed in the Switch-II region from residues Tyr58 to Asp69. The RMSF values increased to 2.8 and 2.6 Å for cis- and trans-KRASNO, and comparable to those from simulations with GDP in the active site. S-nitrosylation had a marginal effect on the flexibility/rigidification of the rest of the residues. Also, the flexibility of loop E (Cys118 to Asp126) where Cys118 residues was less affected from the NO attachment compared to Loop B and Loop C regions.

The calculated RMSF values at 300 K superimposed onto the experimentally measured C_α B-factors and results are shown in Figure S1. For direct comparison, the B-Factor and RMSF values are scaled and normalized. The computed RMSF values for WT agree qualitative with the experimental B-factors except for Switch-II and Helix B region (Tyr58 to Gly77). The agreement between experiment and simulation remains consistent until His27 which is the end residue of Helix A. Similar to WT simulations, an agreement was observed between the experiment and simulations for cis- and trans-KRASNO except for Switch-II and Helix B region. The agreement again remains consistent until the end of helix A. Additionally, agreement from the beginning of Sheet E to the C-terminus of the protein is found for the nitrosylated variants. The lack of agreement for the Switch-II and Helix B region could be due to the fact that two chains are present in the crystal structure compared to using a single chain in the simulations. The differences between experiments and simulations also may arise from effects such as crystal packing or lattice disorder which would not be present in simulations.⁴⁸

Table 1: The average C_α RMSD (in Å) for Sheet D, Sheet E, Sheet F, Helix C, Helix D, Helix E, Loop B, Loop E and the entire protein for WT, cis-KRASNO and trans-KRASNO with respect to the WT X-Ray structure for the last nanosecond of a 10 ns free dynamics simulation at 300 K with PC.

	WT	cis	trans
Sheet D	0.47	0.57	0.56
Sheet E	0.36	0.60	0.43
Sheet F	0.46	0.66	0.40
Helix C	0.99	1.15	1.07
Helix D	0.77	0.95	0.70
Helix E	0.91	1.45	1.87
Loop B	0.89	4.42	1.17
Loop E	1.53	0.85	0.72
Protein	1.28	1.75	1.53

The last nanosecond of the 10 ns production run was analyzed to characterize the structural changes at 300 K. Even though the structural changes induced by the modification were evident for the entire protein structure to a certain degree, eight regions revealed eminent changes. These are: sheet D [Ser65,Glu76], sheet E (Val112 to Lys117), sheet F (Ile142 to Tyr144), helix C (Tyr87 to Ser106), helix D (Tyr127 to Ile139), helix E (Val152 to Lys169), loop B (Ser39 to Asp47) and Loop E (Cys118 to Asp126). The average C_α RMSD (in Å) for these 8 regions and the entire protein for WT, cis-KRASNO and trans-KRASNO with respect to the WT X-Ray structure for the last nanosecond of a 10 ns free dynamics simulation at 300 K with PC are summarized in Table 1 for simulations with GDP.

The effect of the modification to the global structure of the protein was more evident at 300 K, as expected. The RMSD increased by 0.47 and 0.25 Å for cis- and trans-KRASNO with respect to WT, respectively. However, the most dramatic increase in C_α RMSD was observed for loop B in cis-KRASNO, see Section 3.2. The displacement increased to 4.42 Å from 0.89 Å in WT. Since, loop B is also the Switch-I part of the protein, this increase in displacement after S-nitrosylation can have a significant effect on the binding interface characteristics of KRAS to effector proteins and RAS regulators. Also, loop E, where Cys118

resides, is rigidified by the modification the RMSD values are decreased in half for cis- and trans-KRASNO compared to WT.

Table 2: The average C_α RMSD (in Å) for helix F, helix G, helix H, loop B, loop E and chain β_1 for cis- T_0 NO, trans- T_0 NO, T_0 , cis- R_4 NO, trans- R_4 NO, R_4 with respect to the T_0 and R_4 X-Ray structures for the last nanosecond of a 10 ns free dynamics simulation at 300 K with PC and MTP models.

	cis- T_0 NO		trans- T_0 NO		T_0	cis- R_4 NO		trans- R_4 NO		R_4
	PC	MTP	PC	MTP	PC	PC	MTP	PC	MTP	PC
helix F	1.19	1.23	1.23	1.26	1.08	1.48	1.49	1.71	1.71	1.80
helix G	1.30	1.28	1.47	1.46	0.98	1.66	1.68	0.98	0.99	1.35
helix H	1.17	1.16	1.34	1.26	1.26	1.15	1.14	1.24	1.32	1.42
loop B	2.24	2.18	1.97	2.00	1.24	0.96	1.01	0.96	0.99	0.88
loop E	1.66	1.60	1.61	1.66	0.77	1.14	1.28	0.91	0.95	0.74
Chain β_1	0.98	0.98	1.19	1.21	0.93	0.95	0.95	1.04	1.05	0.80

Hemoglobin: The RMSD for the T_0 and R_4 structural substates of hemoglobin with S-nitrosylation at Cys93 β , located on helix F, for both, the cis-, and trans-conformers was considered next. The C_α atoms for cis- $[T_0, R_4]$ NO (orange), and trans- $[T_0, R_4]$ NO (indigo) were superimposed on the $[T_0, R_4]$ (cyan) X-Ray structure at 300 K, see Figure S2. The average C_α RMSD for helix F, helix G, helix H, loop B, loop E and chain β_1 at 300 K are shown in Table 2 for the T_0 and R_4 states. For T_0 the C_α RMSD of Chain β_1 for cis- and trans- T_0 NO with respect to T_0 X-Ray structure are 0.98, 1.19 Å with PC and 0.98, 1.21 Å with MTP, respectively. For the secondary structural motifs, the modification increased the C_α RMSD with respect to T_0 state for helix F, helix G, loop B and loop E. In general the RMSD increases more for trans- T_0 NO than for cis- T_0 NO. The increase in RMSD was marginal for helix G whereas significant increased have been observed for helix G, loop B, loop E. The RMSD increased by 1 Å in cis- conformer with respect to T_0 with PC. The RMSD of loop B was 2.24 Å in cis- conformer and 1.25 Å in T_0 with PC whereas it was 2.18 Å for cis- with MTP. Also, significant increased have been observed for the trans- T_0 NO as well. The RMSD increased to 1.97 Å with PC and 2.00 Å with MTP. For loop E, RMSD

also increased ~ 0.9 Å for S-Nitrosylated variants with respect to T_0 for both PC, and MTP.

For the R_4 state, the C_α RMSD of Chain β_1 for cis- and trans- R_4 NO with respect to R_4 X-Ray structure are 0.98, 1.48 Å with PC and 1.48, 1.54 Å with MTP, respectively. The RMSD of helix F and helix H decreased after the modification for both conformers. For helix G, there was a significant increase in cis- R_4 NO with respect to R_4 with the values of 1.66 and 1.36 Å, respectively, whereas trans- R_4 NO rigidified, and RMSD decreased to 0.982 with PC values. The loop B showed slightly more displacement in both nitrosylated variants compared to R_4 state. No significant deviation between PC and MTP C_α RMSD values have been observed, the highest deviation was 0.08 Å increase for helix H in trans- R_4 NO.

3.2 Dynamical Cross Correlation Maps

To further analyze the effects of -SNO modification, dynamical cross correlation maps (DCCM) and their differences (Δ DCCM) were determined. Difference maps were calculated for cis-KRASNO (Δ DCCM_{cis}) and trans-KRASNO (Δ DCCM_{trans}) with WT as the reference and are shown in Figure 3. The WT DCCM was selected as a reference for Δ DCCM to report on pronounced differences between modified and unmodified proteins and are presented in Figure 3. For Hb, Δ DCCM for [cis, trans]- T_0 NO with T_0 as the reference, and similarly Δ DCCM for [cis, trans]- R_4 NO with R_4 as the reference are presented in Figure 4.

KRAS: For the simulations without GDP, both Δ DCCM_{cis} and Δ DCCM_{trans} had limited number of correlated motions between the different local parts of the protein compared to the simulations with GDP, see Figure 3. The residues mainly had correlated movements within their local part with adjacent residues, except for feature G which labels the correlated motions between sheet B and helix B.

For simulations with GDP, $\Delta\text{DCCM}_{\text{cis}}$, feature A corresponds to correlated movements between helix C and helix D with $0.25 \leq C_{ij} \leq 0.75$. Also, the correlated movement of the Switch-I region with multiple regions such as helix C, loop D, and loop F was observed in feature B. The results show that nitrosylation not only increased the C_α RMSD of Switch-I but also its displacement started to correlate with other local parts of the protein. Especially, the correlated movement between the Switch-I region and helix C shows that residues both can be correlated locally or through space. For $\Delta\text{DCCM}_{\text{trans}}$, correlated motion between helix C and helix D was observed with higher intensity in feature C. Helix C [Tyr87,Ser106] has correlated motions with loop F [Glu107,Met111] (feature D) whereas Helix C has anti-correlated motions with residues from sheet A [Met1,Gly10] to sheet D [Phe78,Ile84]. Also, features E and F show that loop C is involved in anti-correlated motions with residues [Gln70,Phe90] and [Leu120,Pro140], respectively.

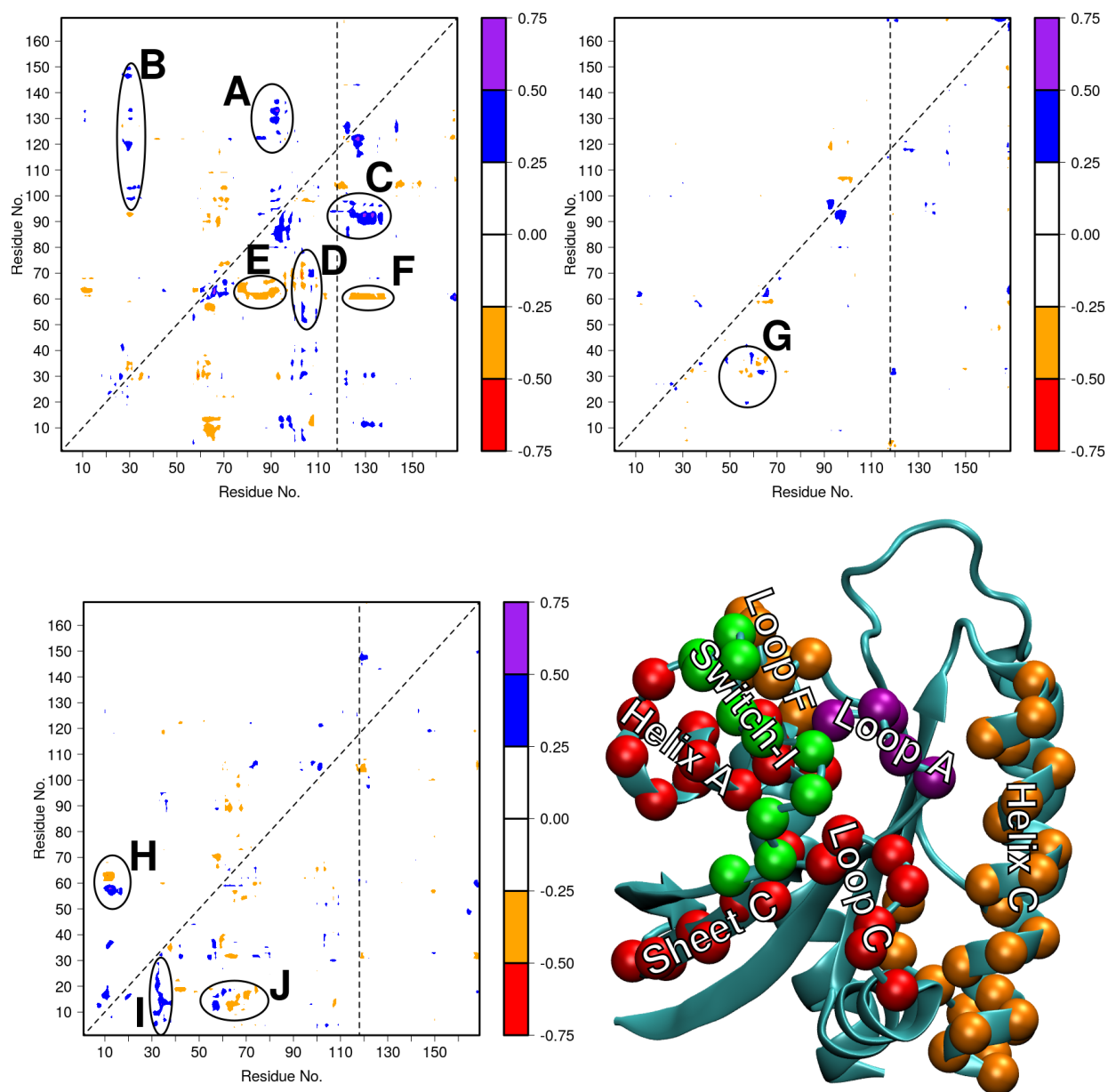


Figure 3: Top left panel: Δ DCCM for GDP-bound KRAS from simulations at 300 K. Left upper triangle reports difference between cis-KRASNO and WT; right lower triangle reports difference between trans-KRASNO and WT. Top right panel: Δ DCCM for ligand-free KRAS from simulations at 300 K. Left upper triangle reports difference between cis-KRASNO and WT; right lower triangle reports difference between trans-KRASNO and WT. The vertical and horizontal lines indicate the position of Cys118. Particular features in the maps are labeled from A to G with circles around them. Bottom left panel: Δ DCCM for cis-KRASNO with and without GDP (left upper triangle) and trans-KRASNO with and without GDP (right lower triangle) at 300 K. The vertical and horizontal lines indicate the position of Cys118. Bottom right panel: Features B (Switch-I in green, and helix C loop D, loop F in orange) and H (Loop A in purple, and helix A, sheet C, loop C in red) visualized on KRAS.

To quantify the effects of the removal of GDP, Δ DCCM are calculated between cis-/trans-KRASNO with and without GDP, and the results are shown in Figure 3. For the cis-isomer, feature H shows correlated motions between loop A with helix A and sheet C whereas there are anti-correlated motions with loop C. Since the diphosphate part of GDP resides near loop A and helix A, the motion of these regions is important for the local dynamics of the protein. Similar features but with larger correlation coefficients were also observed for trans-KRASNO. Feature I shows prominent correlated motion between sheet B and residues from Lys5 to Asp30 (sheet A, loop A, and helix A) whereas sheet C had correlated motions with loop A and helix A and loop C showed anti-correlated motions with these regions, see Feature J.

Overall, the DCCM maps show that S-nitrosylation not only has a significant effect on individual displacements of local structures but also influence local correlated motions. Several correlated motion features were observed in all systems, but they extend over up to 40 residues and the magnitude of the correlation increased after the modification, especially for trans-KRASNO. Lastly, the removal of GDP decreased the correlated motions significantly which emphasizes the dynamical effects induced by ligand binding to the KRAS protein.

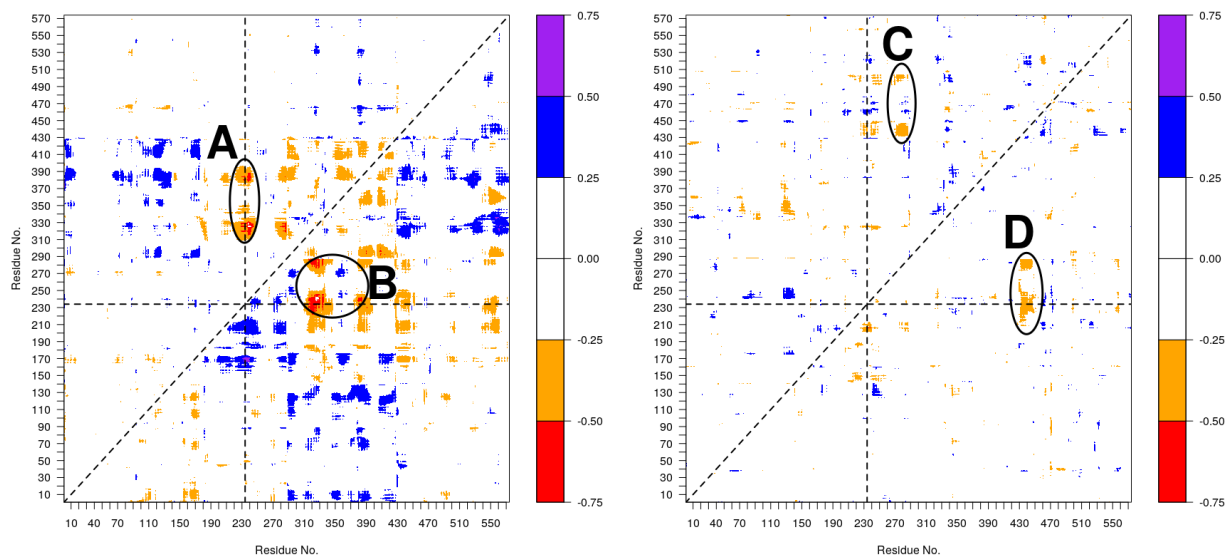


Figure 4: Left panel: Δ DCCM for cis- T_0 NO and T_0 (left upper triangle) and trans- T_0 NO and T_0 (right lower triangle) at 300 K. Right panel: Δ DCCM for cis- R_4 NO and R_4 (left upper triangle) and trans- R_4 NO and R_4 (right lower triangle) at 300 K. Particular features in the maps are labeled from A to D with circles around them.

Hemoglobin: Δ DCCMs are calculated for cis- T_0 NO and T_0 , trans- T_0 NO and T_0 , cis- R_4 NO and R_4 , trans- R_4 NO and R_4 , and presented in Figure 4. The structural motions were significantly more correlated for T_0 NO compared to R_4 NO. The anti-correlated motions which have $C_{ij} \leq -0.75$ were observed for both cis- and trans- T_0 NO. Two particular features are labeled in T_0 , see left panel of Figure 4. Feature A shows the anti-correlated motions between [Leu87B,Leu115B] (including the modified Cys93 β residue), and [Ala28C,Tyr42C] in cis- T_0 NO. Feature B shows strong anti-correlated motions between [Ala28C,Leu48C] and [Asp79B,Arg104B] in trans- T_0 NO. For R_4 proteins motions were less correlated and have values between $-0.50 \leq C_{ij} \leq 0.50$. In feature C, there were anti-correlated motions between [Thr4D,Glu22D] and [Ala70B,Leu114B] in cis- R_4 NO. Similarly, feature D showed anti-correlated motions between [Ala129B,His146B] and [Leu3D,Val20D] in trans- R_4 NO. Overall, the correlated motions were mostly between chain β_1 (including Cys93NO) and chain C. The results emphasize the effect of the modification on the correlated motions of Hb protein.

3.3 Hydration Structure Around the Modification Site

Next, local hydration around the S-nitrosylated Cys were analyzed by means of radial distribution function, and their corresponding coordination numbers for both KRAS, and Hb. Given the evident role that water can play for the protein function (see Introduction), such a change in hydration may also be functionally relevant for a PTM such as S-nitrosylation.

First, the local water ordering around the modification site (Cys118) for WT and S-nitrosylated KRAS is considered. The radial distribution function $g_{S-OW}(r)$ and the corresponding number $N_{S-OW}(r)$ of water oxygen (OW) with respect to the sulfur atom of Cys118 in WT, cis-KRASNO, and trans-KRASNO are shown for both, simulations with and without GDP in the active site, see Figure 5. Nitrosylated KRAS remained in its starting cis- and trans-conformations, respectively, throughout the 10 ns trajectory. For simulations with GDP at 300 K, hydration around Cys118 substantially differs between WT and cis-, trans-KRASNO in the active site. Both nitrosylated variants were less hydrated around Cys118 in the range of r_{S-OW} between 3 and 5 Å compared with WT. The first solvation shell peak appears at 3.5 Å in WT (see Figure 5, black line) and cis-KRASNO (red line) whereas no sharp first solvation peak was observed for trans-KRASNO (blue line). These results show that the -SNO moiety in the trans-conformation is less solvent-exposed compared to the cis-conformer. The occupation of the first solvation shell (up to $r_{S-OW} \sim 5$) differs by 2 and 3 water molecules, which amounts to 43 and 28%, with respect to WT for cis- and trans-KRASNO, respectively.

For simulations without GDP at 300 K, again, hydration around Cys118 substantially differs between WT and cis-, trans-KRASNO. The nitrosylated variants were less hydrated in the environment of the sulfur atom in the range of r_{S-OW} 3–5 Å compared with WT. However, contrary to the simulations including GDP, trans-SNO was more solvent-exposed and thus had increased hydration compared to cis-SNO. The first solvation shell peak for WT and trans-KRASNO appears at 3.5 Å. The first solvation shell for cis- and trans-KRASNO was

less occupied by 2 and 1 water molecules compared to WT which is a reduction of 40 and 20% for cis- and trans-KRASNO, respectively.

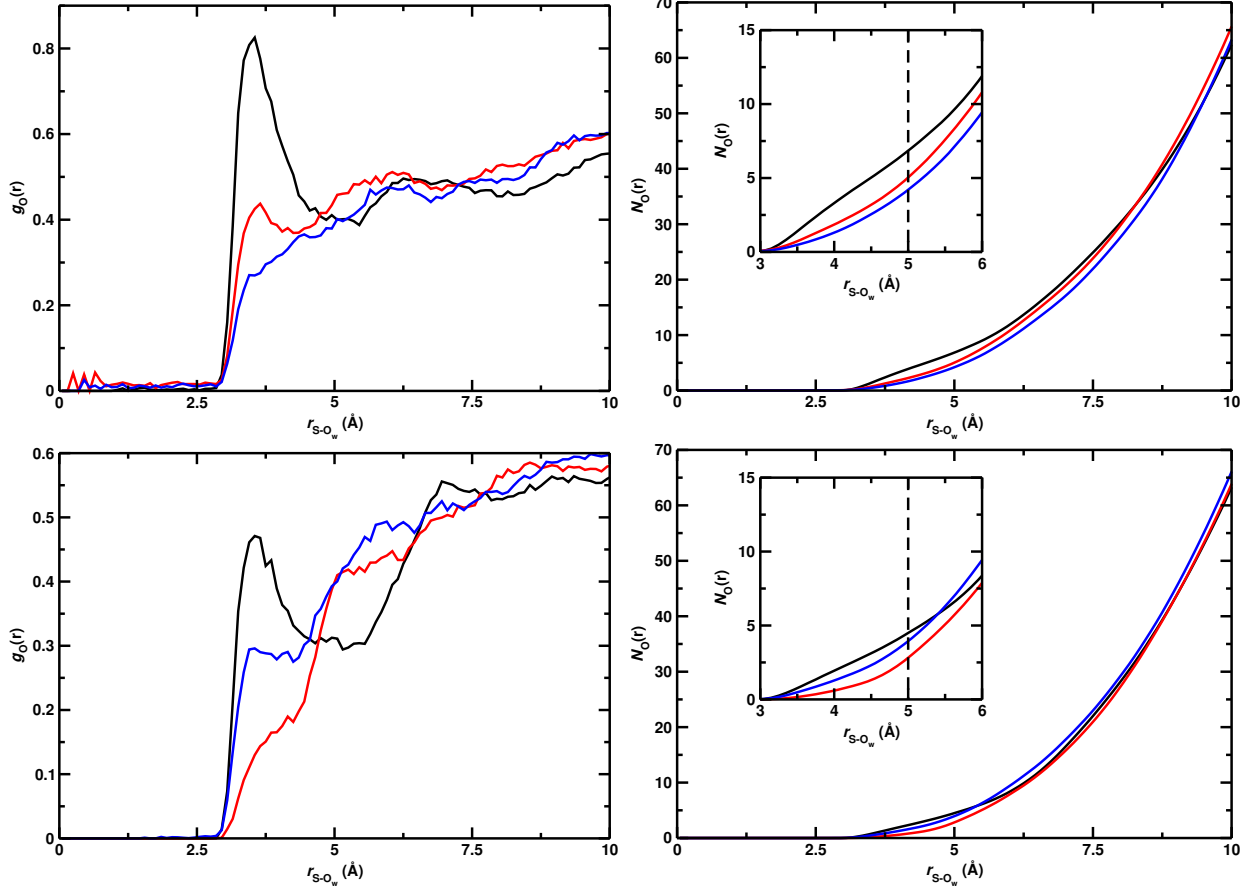


Figure 5: Top Panels: Radial distribution function of water oxygen (Left) and the corresponding coordination number of $N_O(r)$ of water oxygen (Right) with respect to the sulfur atom obtained from NpT simulations for KRAS with GDP bound at 300 K using point charges. Bottom Panels: For the simulations without GDP, the radial distribution function of water oxygen (Left) and the corresponding coordination number of $N_O(r)$ of water oxygen (Right) with respect to the sulfur atom obtained from NpT simulations at 300 K with PC model. Color code: WT (black), cis-KRASNO (red), trans-KRASNO (blue).

The number of water molecules within 5 Å of the phosphate atoms of GDP (P_{GDP}) in WT, cis- and trans-KRASNO at 300 K as a function of time is shown in Figure S3. The phosphate side of the GDP selected for the analysis for two reasons: first, electron rich phosphate atoms engage in electrostatic interactions with water molecules, hence push or collect water molecules in their vicinity and secondly, the chemically important part of the GDP where

reactions such as phosphate transfer take place. The hydration around P_{GDP} is drastically decreased in cis-KRASNO compared to WT and trans-KRASNO. The average number of water molecules was 7.2, 3.7 and 7.0 for WT, cis- and trans-KRASNO, respectively. The decrease in hydration can be rationalized by the increased displacement of the Switch-I region (Phe28 to Asp38) near GDP in cis-KRASNO compared to the WT X-Ray structure and WT, trans-KRASNO simulations, (see Table 1) which pushed the water molecules away from the P_{GDP} .

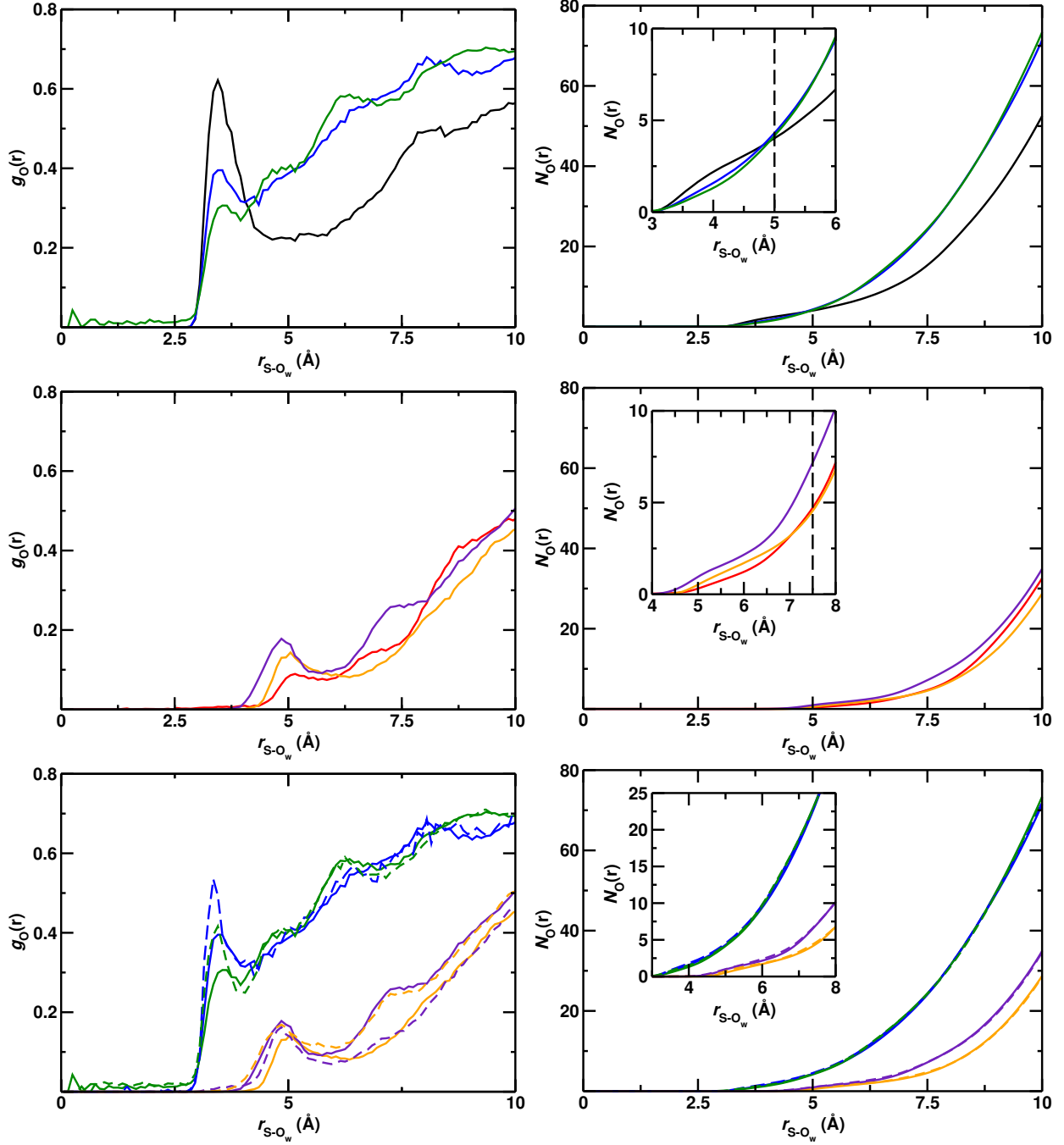


Figure 6: Water structure around Hb, left column for radial distribution functions (with respect to sulfur atom of Cys93) and right column for total number of water molecules from NpT simulations at 300 K. Top Panel: T_0 (black), cis- $T_0\text{NO}$ (blue), trans- $T_0\text{NO}$ (green) from PC simulations. Middle Panels) R_4 (red), cis- $R_4\text{NO}$ (orange), and trans- $R_4\text{NO}$ (indigo) from PC simulations. Bottom Panels: Solid lines are for PC, dashed lines are for MTP. Color code: cis- $T_0\text{NO}$ (blue), trans- $T_0\text{NO}$ (green), cis- $R_4\text{NO}$ (orange), and trans- $R_4\text{NO}$ (indigo).

Hemoglobin: Next, the hydration near the NO- modification site (Cys93 β) is considered for

WT and S-nitrosylated HbNO is investigated. The radial distribution function $g_{S-OW}(r)$ and the corresponding number $N_{S-OW}(r)$ of water oxygen (OW) with respect to the sulfur atom of Cys93 β in WT, cis-HbNO, and trans-HbNO are shown for both T₀NO and R₄NO states with PC in Figures 6. For the T₀NO state, hydration at 300 K decreases significantly after the modification for the first solvation shell, especially in trans-T₀NO. The first solvation shell was observed at 3.5 Å for all variants. However, beyond the first solvation shell, both cis- and trans-T₀NO draw more water molecules around themselves. The same number of water molecules was observed at 5 Å for all variants, however, for distances larger than 5 Å number of water molecules increased for the nitrosylated proteins. The results show that S-nitrosylation pushed waters away in the first solvation shell but recruit more water after 5 Å compared to WT. For the R₄NO state, hydration around Cys93 β was substantially lowered compared to T₀NO. The Cys93 β was less solvent-exposed in R₄NO and peaks were lower in magnitude. Further, the first solvation shell peak was observed at 5 Å. Contrary to T₀NO, the S-nitrosylation deepens the first solvation shell in R₄NO for both cis-, and trans-R₄NO. The difference in the total number of water between WT and modified proteins at 7.5 Å was lower in the R₄NO state.

Multipoles up to quadrupoles were also added to the conventional point charges to determine the effects of more accurate electrostatic model to the quantification of the local hydration. The radial distribution function $g_{S-OW}(r)$ and the corresponding number $N_{S-OW}(r)$ of water oxygen (OW) with respect to the sulfur atom of Cys93 β in cis-HbNO, and trans-HbNO are shown for both T₀NO and R₄NO states with PC and MTP in Figures 6. For the T₀NO state, the local hydration increased with MTP model for both cis- and trans-T₀NO compared to PC. The first solvation shells around 3 Å were deeper. However, the difference between PC and MTP is diminished after 4.5 Å. For R₄NO state, the effect of additional multiples was marginal compared to PC. The number of water molecules around the Cys93 β did not change between the models.

Small peaks at 0 to 2.75 Å before the first solvation shell, starting at 2.75 Å were observed for the $g_O(r)$ of trans-T₀NO, which is not present in other proteins, see Figures 6. To further characterize these peaks, a total number of waters 2.75 Å around the Cys93β as a function of time is computed, and presented in Figure S4. The total number of water molecules ranged from 1 to 12 throughout the trajectory. The substantial changes in the total number indicate a migration (or diffusion) of water. Especially, a decrease in hydration after 8 ns was present. On average 5 water molecules were around 2.75 Å of Cys93β.

3.4 Local Hydrophobicity Analysis

In this section, the local hydrophobicity (LH) around the S-nitrosylated Cys118 for KRAS and Cys93β for Hb proteins are investigated. LH ($\delta\lambda_{phob}^r(t)$) is time-dependent quantity to determine and quantify solvent exposure of a given amino acid residue r at time t . LH is a quantity that can be considered as a prolongation of the radial distribution function, which encompasses both orientation of a given water molecule and its distance from the interface into consideration. In this study, the probability density function of $\delta\lambda_{phob}^r(t)$ is present and positive LH values ($\delta\lambda_{phob}^r > 0$) considered as indicative for hydrophilicity.

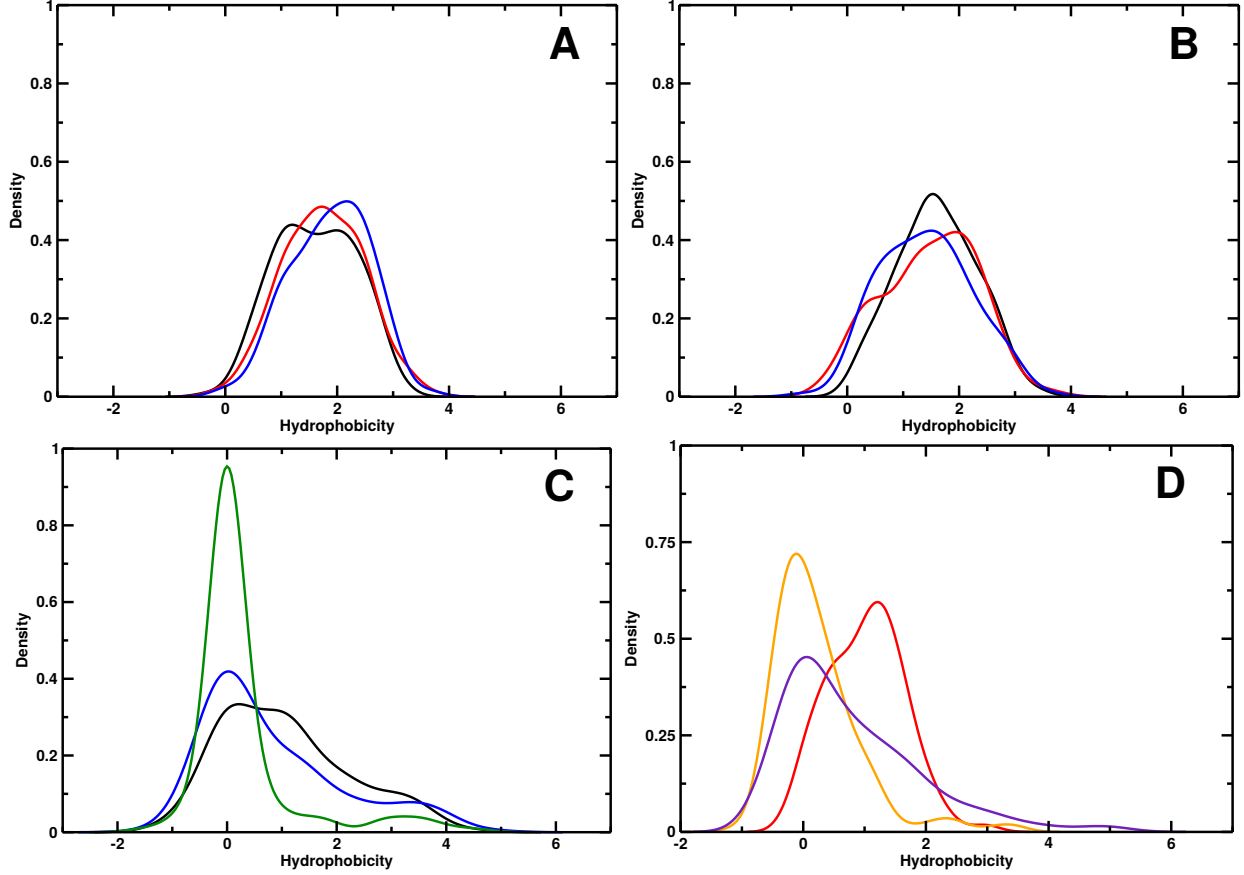


Figure 7: Panel A: The distribution of hydrophobicity values of Cys118 from 10 ns NpT simulations at 300 K for WT KRAS (black), cis-KRASNO (red), and trans-KRASNO (blue). Panel B: The distribution of hydrophobicity values of Cys118 from 10 ns NpT simulations at 300 K for WT KRAS without GDP (black), cis-KRASNO without GDP (red), and trans-KRASNO without GDP (blue). C) The distribution of hydrophobicity values of Cys93 β from 10 ns NpT simulations at 300 K for T₀ (black), cis-T₀NO (blue), and trans-T₀NO (green). D) The distribution of hydrophobicity values of Cys93 β from 10 ns NpT simulations at 300 K for R₄ (red), cis-R₄NO (orange), and trans-R₄NO (indigo)

KRAS: The distribution of hydrophobicity values of Cys118 for WT KRAS (black), cis-KRASNO (blue), and trans-KRASNO (green) is shown in Figure 7A, and WT KRAS without GDP (black), cis-KRASNO without GDP (blue), and trans-KRASNO without GDP (green) shown in Figure 7B. For the simulations with GDP (see Panel A), the hydrophobicity distributions were similar for all KRAS variants. They had a broad density peak for LH between [0,4] which emphasizes the strong hydrophilic character of Cys118 residue. The highest density points for cis-KRASNO were at 1.8 whereas 2.1 for trans-KRASNO. The

WT KRAS had multimodal distribution with density maxima at 1 and 2.1. For simulations without GDP (see Panel B), again all variants showed strong hydrophilic character with a broad density peak between [0,4]. The WT KRAS without GDP had monomodal distribution, whereas cis-KRASNO had a shoulder around 0. The highest density points were between [1.9, 2.1] for all variants.

Hemoglobin: The distribution of hydrophobicity values of Cys93 β for T₀ (black), cis-T₀NO (blue), trans-T₀NO (green), R₄ (red), cis-R₄NO (orange), and trans-R₄NO (indigo) shown in Figure 7. The T₀ (Panel A) had the highest density in [0, 1.5] regions and had positive skew distribution which means T₀ had mostly hydrophilic character. Although S-nitrosylated variants also showed some hydrophilic characters, the highest density values for both cis- and trans- conformers were closer to 0. The cis-T₀NO had positive skew distribution similar to T₀, the highest density observed at 0. However, the positive skew emphasizes the hydrophilic character. The trans-T₀NO had the highest density around in [-1, 1] with a second density maximum around 3, which means it shows mostly hydrophobic character throughout the simulation compared to T₀.

For R₄ (Panel B), the density maximum was at 1.7, and the distribution had a shoulder around 0.5. Although it had negative skew, distributed values were mostly positive emphasizing a strong hydrophilic character. The density maxima for the S-nitrosylated variants were at 0, and both had positive skews. Both cis- and trans- conformers showed less hydrophilic character compared to R₄. A similar trend was also observed in T₀ proteins.

3.5 Infrared Spectroscopy in the -NO Stretch Region

One direct way to detect whether or not nitrosylation occurred, is by the use of infrared spectroscopy. The IR and power spectra for nitrosylated KRAS and Hb are presented in

Figures 8 and S5, respectively.

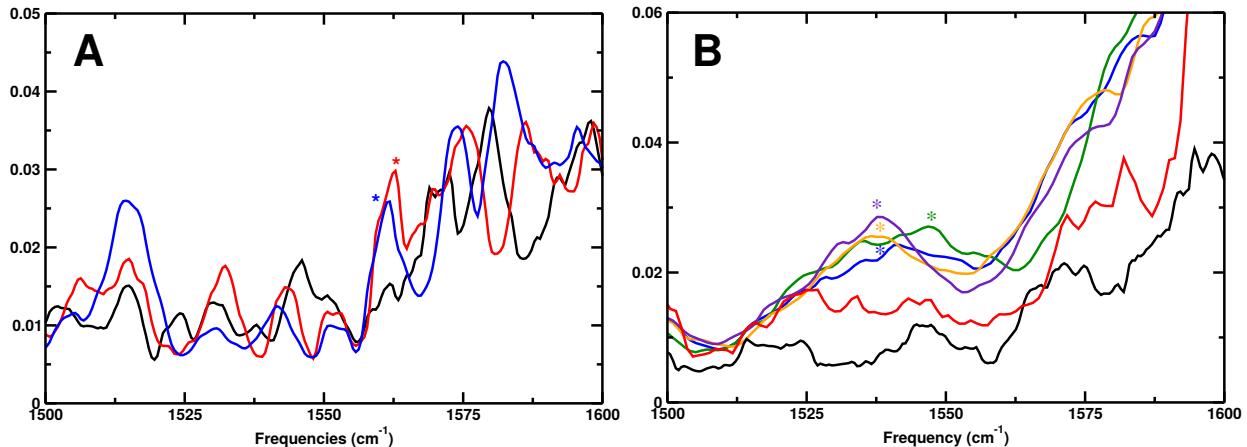


Figure 8: Panel A: IR spectra from the total protein dipole moment time series for WT without GDP (black), cis-KRASNO with GDP (red), and trans-KRASNO with GDP at 50 K. The $^{14}\text{N}^{18}\text{O}$ isotope is used for the cis- and trans-KRASNO. Panel B: IR spectra for Hb, T_0 (black), R_4 (red), cis- T_0NO (blue), trans- T_0NO (green), cis- R_4NO (orange), and trans- R_4NO (indigo). Spectra are range between 1500 and 1600 cm^{-1} presented. The colored stars label the spectral signatures to which the mode was assigned based on analysis of the power spectra.

KRAS: For KRAS, determining the IR band due to the NO stretch for the natural isotope was not possible due to congested spectra in the amide I region. Thus, the IR spectra related to the $^{14}\text{N}^{18}\text{O}$ stretch are reported in Figure 8 for WT (black), cis- and trans-KRASNO (red, blue) with GDP at 50 K. Such a low temperature was required to avoid washing out the peak that belongs to the NO-stretch. For the $^{14}\text{N}^{18}\text{O}$ stretch, the peak for cis-KRASNO from the simulations appears at 1561 cm^{-1} compared with 1563 cm^{-1} for trans-KRASNO. Also, the peak intensity was higher for the trans variant with respect to cis. The assignment of these peaks is also possible by considering the power spectra corresponding to the NO stretch motion. The power spectra of cis-KRASNO with $^{14}\text{N}^{16}\text{O}$ (black), $^{14}\text{N}^{18}\text{O}$ (red) and $^{15}\text{N}^{18}\text{O}$ (blue). trans-KRASNO with $^{14}\text{N}^{16}\text{O}$ (green), $^{14}\text{N}^{18}\text{O}$ (yellow) and $^{15}\text{N}^{18}\text{O}$ (magenta) has shown in Figure S5. The identical simulations for all three isotopic variants lead to red-shifts of the $^{14}\text{N}^{18}\text{O}$ -stretch by $[-27, -20]$ cm^{-1} for [cis,trans]-KRASNO and $^{15}\text{N}^{18}\text{O}$ -stretch by $[-59, -61]$ cm^{-1} for [cis,trans]-KRASNO compared to the natural isotope $^{14}\text{N}^{16}\text{O}$. The

red-shifts observed for the isotopic substitution are on par with previous examples.²⁹

Hemoglobin: For Hb, the NO peak was observed with the natural isotope, and IR spectra related to NO stretch are reported in Figure 8 for cis-T₀NO, trans-T₀NO, cis-R₄NO, and trans-R₄NO at 50 K. The peak for [cis,trans]-T₀NO appears at [1540,1547] cm⁻¹ whereas for [cis,trans]-R₄NO appears at [1537,1538]. The results show that R₄NO variants are red-shifted by 3 and 9 cm⁻¹ compared to cis- and trans-T₀NO, respectively. Further, trans-conformers were blue-shifted by 7 and 1 cm⁻¹ compared to cis- conformers for both T₀NO and R₄NO. The shifts show that cis, trans- conformers, especially for T₀NO, and T₀NO, R₄NO proteins can be distinguished with IR spectra.

4 Conclusions

The present work reports on the structural, dynamical, hydration, and spectroscopic implications of nitrosylation of cysteine residues. For this, S-nitrosylated KRAS without and with GDP, and the T₀ and R₄ structural substates of Hb were considered. The overall finding is that nitrosylation influences local hydration, and the local and global dynamics of the proteins. More specifically, for KRAS it was found that attaching NO to Cys118 rigidifies the Switch-I region which has functional implications because this region acts as a binding interface for effector proteins and RAS regulators. On the other hand, for Hb in its T₀ and R₄ substates the flexibility of secondary structural motives was increased following S-nitrosylation. These effects were confirmed from analyzing DCCM maps which imply that correlated movements between the switch-I region and nearby helix C increase for KRASNO. Similarly, for Hb the amplitude of correlated motions increased for T₀NO compared with R₄NO.

For local hydration it is found that S-nitrosylation in KRAS decreases water access by up to 40 %. Also, cis- versus trans-orientations of the modifications lead to different local hydration. This is also found for T_0NO and R_4NO with the additional observation that for the R_4 conformation the hydration is yet lower than for the T_0NO substate. Finally, the infrared spectra in the NO stretch region were determined and were found to exhibit characteristic peaks and shifts depending the ligation state (for KRAS) or conformational substate. However, the absorption occurs in a spectrally congested region of the protein-IR spectrum which will make experimental detection of these bands difficult.

In conclusion, for KRAS and Hb considered in the present work the simulations find characteristic differences between WT and nitrosylated variants of the proteins with regards to local hydration and local and global flexibility of the proteins. This, together with earlier finding for Mb, suggests that attaching NO to cysteine residues at the surface of proteins has functional implications.

Supporting Information

The supporting information provides RMSD and power spectra.

5 Acknowledgment

This work was supported by the Swiss National Science Foundation grants 200021-117810, 200020-188724, the NCCR MUST, and the University of Basel which is gratefully acknowledged.

References

- (1) Walsh, C. *Posttranslational Modification of Proteins: Expanding Nature's Inventory*; Roberts and Company Publishers, 2006.
- (2) Scott, J. D.; Pawson, T. Cell Signaling in Space and Time: Where Proteins Come Together and When They're Apart. *Science* **2009**, *326*, 1220–1224.
- (3) Nussinov, R.; Tsai, C.-J.; Xin, F.; Radivojac, P. Allosteric Post-Translational Modification Codes. *Trends Biochem. Sci.* **2012**, *37*, 447–455.
- (4) Walsh, C. T.; Garneau-Tsodikova, S.; Gatto Jr, G. J. Protein Post-translational Modifications: the Chemistry of Proteome Diversifications. *Angew. Chem. Int. Ed.* **2005**, *44*, 7342–7372.
- (5) Walsh, C. T.; Malcolmson, S. J.; Young, T. S. Three Ring Post-translational Circuses: Insertion of Oxazoles, Thiazoles, and Pyridines into Protein-derived Frameworks. *ACS Chem. Biol* **2017**, *7*, 429–442.
- (6) Van Der Velden, N. S.; Kälin, N.; Helf, M. J.; Piel, J.; Freeman, M. F.; Künzler, M. Autocatalytic Backbone N-methylation in a Family of Ribosomal Peptide Natural Products. *Nat. Chem. Biol* **2017**, *13*, 833–835.
- (7) Burkhardt, B. J.; Schwalen, C. J.; Mann, G.; Naismith, J. H.; Mitchell, D. A. YcaO-dependent Post-translational Amide Activation: Biosynthesis, Structure, and Function. *Chem. Rev.* **2017**, *117*, 5389–5456.
- (8) Jaffrey, S. R.; Erdjument-Bromage, H.; Ferris, C. D.; Tempst, P.; Snyder, S. H. Protein S-nitrosylation: a physiological signal for neuronal nitric oxide. *Nat. Cell Biol.* **2001**, *3*, 193–197.
- (9) Voller, A.; Bartlett, A.; Bidwell, D. Enzyme Immunoassays with Special Reference to ELISA Techniques. *J. Clin. Pathol.* **1978**, *31*, 507–520.

- (10) Alcock, L. J.; Perkins, M. V.; Chalker, J. M. Chemical methods for mapping cysteine oxidation. *Chem. Soc. Rev.* **2018**, *47*, 231–268.
- (11) Doll, S.; Burlingame, A. L. Mass spectrometry-based detection and assignment of protein posttranslational modifications. *ACS chemical biology* **2015**, *10*, 63–71.
- (12) Kumar, A.; Narayanan, V.; Sekhar, A. Characterizing post-translational modifications and their effects on protein conformation using NMR spectroscopy. *Biochemistry* **2019**, *59*, 57–73.
- (13) McLaughlin, R. J.; Spindler, M. P.; van Lummel, M.; Roep, B. O. Where, how, and when: positioning posttranslational modification within type 1 diabetes pathogenesis. *Current diabetes reports* **2016**, *16*, 1–9.
- (14) Wang, Y.-C.; Peterson, S. E.; Loring, J. F. Protein post-translational modifications and regulation of pluripotency in human stem cells. *Cell research* **2014**, *24*, 143–160.
- (15) Case, N.; Thomas, J.; Sen, B.; Styner, M.; Xie, Z.; Galior, K.; Rubin, J. Mechanical regulation of glycogen synthase kinase 3β (GSK3 β) in mesenchymal stem cells is dependent on Akt protein serine 473 phosphorylation via mTORC2 protein. *Journal of Biological Chemistry* **2011**, *286*, 39450–39456.
- (16) Davies, M. J. Protein oxidation and peroxidation. *Biochemical journal* **2016**, *473*, 805–825.
- (17) Hagai, T.; Levy, Y. Ubiquitin not only serves as a tag but also assists degradation by inducing protein unfolding. *Proceedings of the National Academy of Sciences* **2010**, *107*, 2001–2006.
- (18) Simanshu, D. K.; Nissley, D. V.; McCormick, F. RAS proteins and their regulators in human disease. *Cell* **2017**, *170*, 17–33.

- (19) Colicelli, J. Human RAS superfamily proteins and related GTPases. *Science's STKE* **2004**, *2004*, re13–re13.
- (20) Reck, M.; Carbone, D.; Garassino, M.; Barlesi, F. Targeting KRAS in non-small-cell lung cancer: Recent progress and new approaches. *Annals of Oncology* **2021**, *32*, 1101–1110.
- (21) Prior, I. A.; Hood, F. E.; Hartley, J. L. The frequency of Ras mutations in cancer. *Cancer research* **2020**, *80*, 2969–2974.
- (22) Baldwin, J.; Chothia, C. Haemoglobin: the structural changes related to ligand binding and its allosteric mechanism. *Journal of molecular biology* **1979**, *129*, 175–220.
- (23) Denisov, V. P.; Halle, B. Protein hydration dynamics in aqueous solution. *Faraday Discussions* **1996**, *103*, 227–244.
- (24) Halle, B. Protein hydration dynamics in solution: a critical survey. *Philosophical Transactions of the Royal Society of London. Series B: Biological Sciences* **2004**, *359*, 1207–1224.
- (25) Edsall, J. T.; McKenzie, H. A. Water and proteins. II. The location and dynamics of water in protein systems and its relation to their stability and properties. *Advances in biophysics* **1983**, *16*, v–vi.
- (26) Olson, J. S.; Soman, J.; Phillips, G. N. Ligand pathways in myoglobin: A review of trp cavity mutations. *IUBMB Life* **2007**, *59*, 552–562.
- (27) Chen, X.; Weber, I.; Harrison, R. W. Hydration water and bulk water in proteins have distinct properties in radial distributions calculated from 105 atomic resolution crystal structures. *The Journal of Physical Chemistry B* **2008**, *112*, 12073–12080.
- (28) Morón, M. C. Protein hydration shell formation: Dynamics of water in biological systems exhibiting nanoscopic cavities. *Journal of Molecular Liquids* **2021**, *337*, 116584.

- (29) Turan, H. T.; Meuwly, M. Spectroscopy, dynamics, and hydration of S-nitrosylated myoglobin. *The Journal of Physical Chemistry B* **2021**, *125*, 4262–4273.
- (30) Hardin, S. C.; Larue, C. T.; Oh, M.-H.; Jain, V.; Huber, S. C. Coupling oxidative signals to protein phosphorylation via methionine oxidation in Arabidopsis. *Biochemical Journal* **2009**, *422*, 305–312.
- (31) Liu, N.; Guo, Y.; Ning, S.; Duan, M. Phosphorylation regulates the binding of intrinsically disordered proteins via a flexible conformation selection mechanism. *Communications Chemistry* **2020**, *3*, 1–9.
- (32) Moeller, H. B.; Olesen, E. T.; Fenton, R. A. Regulation of the water channel aquaporin-2 by posttranslational modification. *American Journal of Physiology-Renal Physiology* **2011**, *300*, F1062–F1073.
- (33) Brooks, B. R.; Brooks, C. L., III; Mackerell, A. D., Jr.; Nilsson, L.; Petrella, R. J.; Roux, B.; Won, Y.; Archontis, G.; Bartels, C.; Boresch, S. et al. CHARMM: The Biomolecular Simulation Program. *J. Comput. Chem.* **2009**, *30*, 1545–1614.
- (34) Huang, J.; MacKerell Jr, A. D. CHARMM36 all-atom additive protein force field: Validation based on comparison to NMR data. *J. Comput. Chem.* **2013**, *34*, 2135–2145.
- (35) Hairer, E.; Lubich, C.; Wanner, G. Geometric numerical integration illustrated by the Störmer–Verlet method. *Acta Numer.* **2003**, *12*, 399–450.
- (36) Ryckaert, J.-P.; Ciccotti, G.; Berendsen, H. J. Numerical integration of the cartesian equations of motion of a system with constraints: molecular dynamics of n-alkanes. *J. Comput. Phys.* **1977**, *23*, 327–341.
- (37) Steinbach, P. J.; Brooks, B. R. New spherical-cutoff methods for long-range forces in macromolecular simulation. *J. Comput. Chem.* **1994**, *15*, 667–683.

- (38) Darden, T.; York, D.; Pedersen, L. Particle mesh Ewald: An $N\log(N)$ method for Ewald sums in large systems. *J. Chem. Phys.* **1993**, *98*, 10089–10092.
- (39) Hunter, J. C.; Gurbani, D.; Ficarro, S. B.; Carrasco, M. A.; Lim, S. M.; Choi, H. G.; Xie, T.; Marto, J. A.; Chen, Z.; Gray, N. S. et al. In situ selectivity profiling and crystal structure of SML-8-73-1, an active site inhibitor of oncogenic K-Ras G12C. *Proceedings of the National Academy of Sciences* **2014**, *111*, 8895–8900.
- (40) Jorgensen, W. L.; Chandrasekhar, J.; Madura, J. D.; Impey, R. W.; Klein, M. L. Comparison of simple potential functions for simulating liquid water. *J. Chem. Phys.* **1983**, *79*, 926–935.
- (41) Verlet, L. Computer Experiments on Classical Fluids. I. Thermodynamical Properties of Lennard-Jones Molecules. *Phys. Rev.* **1967**, *159*, 98–103.
- (42) Hoover, W. G. Canonical Dynamics: Equilibrium Phase-Space Distributions. *Phys. Rev. A* **1985**, *31*, 1695–1697.
- (43) Lammers, S.; Meuwly, M. Investigating the relationship between infrared spectra of shared protons in different chemical environments: A comparison of protonated diglyme and protonated water dimer. *J. Phys. Chem. A* **2007**, *111*, 1638–1647.
- (44) Ichiye, T.; Karplus, M. Collective motions in proteins: a covariance analysis of atomic fluctuations in molecular dynamics and normal mode simulations. *Proteins: Structure, Function, and Bioinformatics* **1991**, *11*, 205–217.
- (45) Arnold, G. E.; Ornstein, R. L. Molecular dynamics study of time-correlated protein domain motions and molecular flexibility: cytochrome P450BM-3. *Biophysical journal* **1997**, *73*, 1147–1159.
- (46) Grant, B. J.; Rodrigues, A. P.; ElSawy, K. M.; McCammon, J. A.; Caves, L. S. Bio3d:

- an R package for the comparative analysis of protein structures. *Bioinformatics* **2006**, *22*, 2695–2696.
- (47) Pantsar, T. The current understanding of KRAS protein structure and dynamics. *Computational and structural biotechnology journal* **2020**, *18*, 189–198.
- (48) Sun, Z.; Liu, Q.; Qu, G.; Feng, Y.; Reetz, M. T. Utility of B-factors in protein science: interpreting rigidity, flexibility, and internal motion and engineering thermostability. *Chem. Rev.* **2019**, *119*, 1626–1665.

SUPPORTING INFORMATION: Local Hydration Control and Functional Implications Through S-Nitrosylation of Proteins: Kirsten rat sarcoma virus (KRAS) and Hemoglobin (Hb)

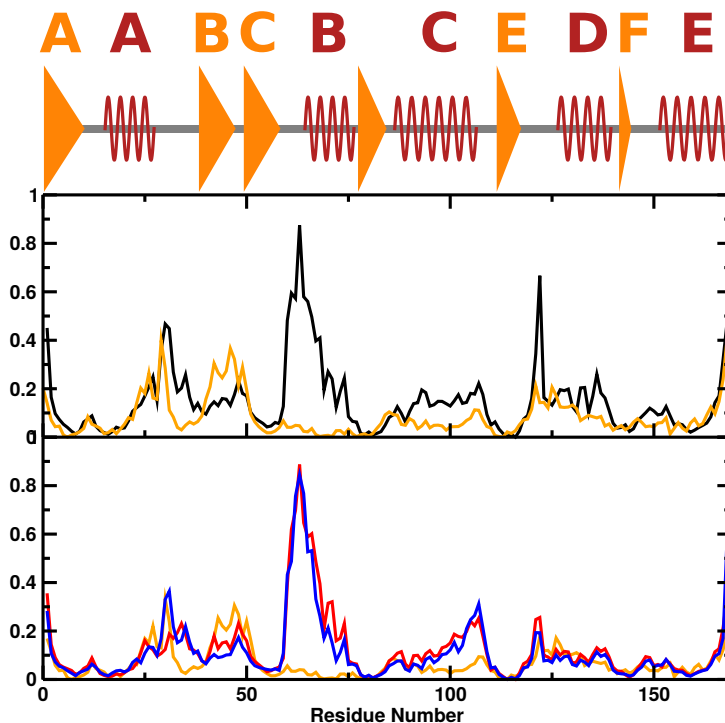


Figure S1: Superposition of the experimentally measured C_{α} B-factors and the computed C_{α} RMSFs from the present simulations. Up) Experimental WT B-Factors (orange) vs. WT (black) RMSF at 300 K. Bottom) WT B-Factors vs cis- (red) and trans-KRASNO (blue) RMSF at 300 K. B-Factor and RMSF values are scaled and normalized. Orange triangles indicate the position of β -sheets and red helices indicate the position of α -helices

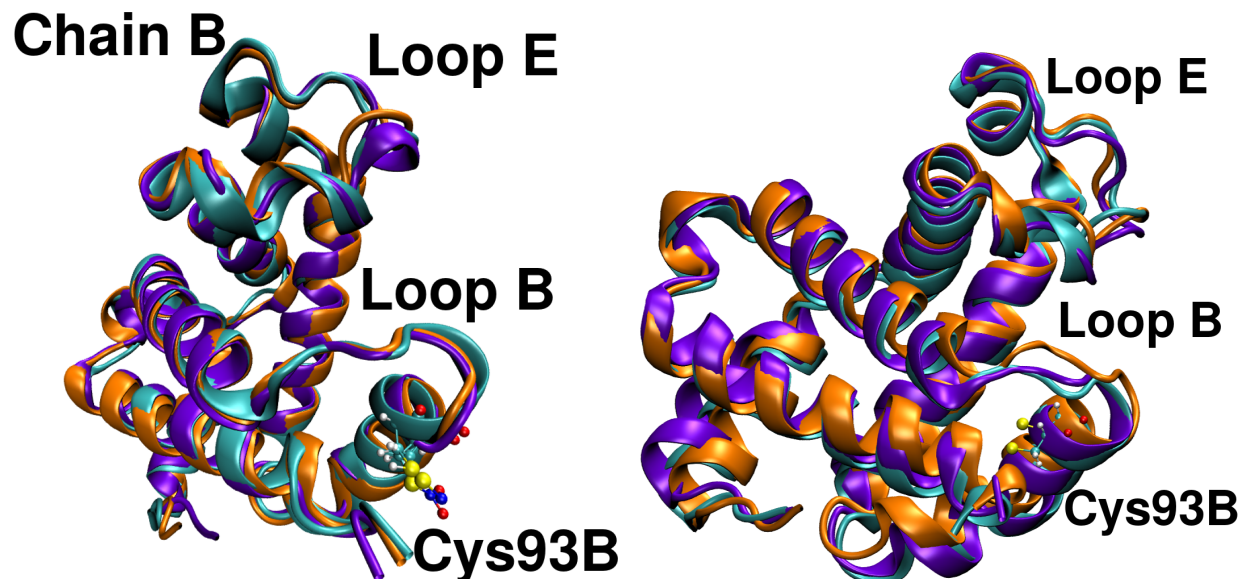


Figure S2: Conformational changes for Hb induced by S-nitrosylation at Cys93 β_1 from simulations at 300 K. Left structure: T₀ (cyan), cis-T₀NO (orange), trans-T₀NO (indigo). Right structure: R₄ (cyan), cis-R₄NO (orange), trans-R₄NO (indigo) S-nitrosylated Cys93 β is represented by CPK.

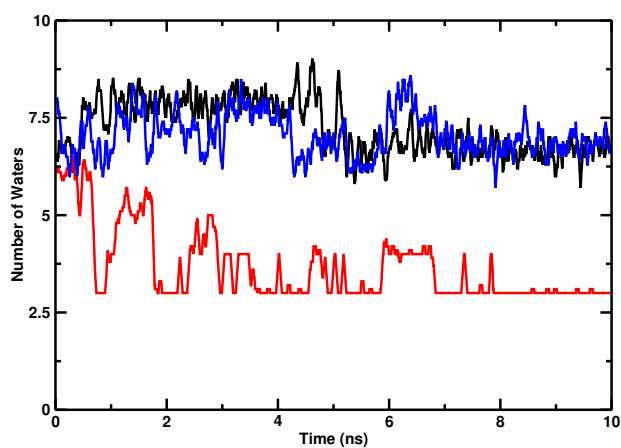


Figure S3: The number of water molecules within 5 Å of the phosphate atoms of GDP in WT (black), cis- (red) and trans-KRASNO (blue) at 300 K as a function of time.

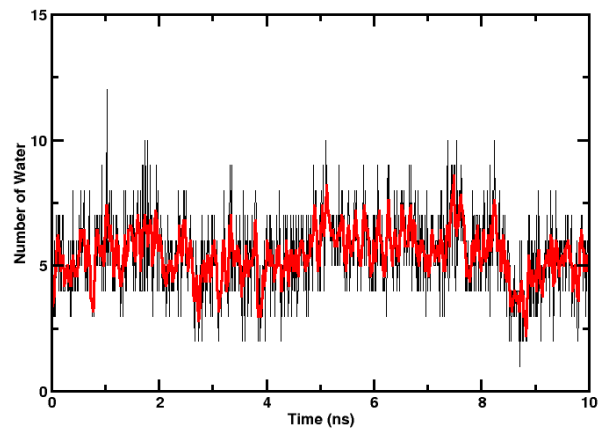


Figure S4: The number of solvent water molecules within 2.75 Å of the Cys93B in trans-T₀NO at 300 K from simulations with point charges.

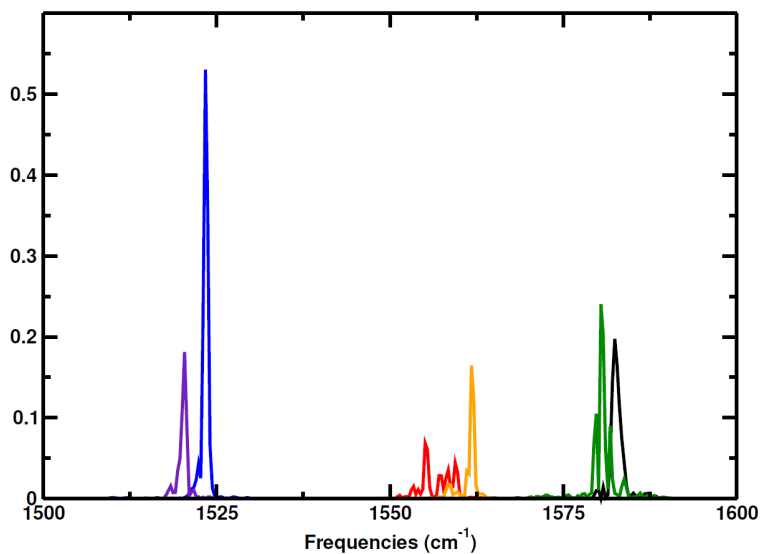


Figure S5: The power spectra for cis- and trans-KRASNO at 50 K. Color code: cis-KRASNO with $^{14}\text{N}^{16}\text{O}$ (black), $^{14}\text{N}^{18}\text{O}$ (red) and $^{15}\text{N}^{18}\text{O}$ (blue). trans-KRASNO with $^{14}\text{N}^{16}\text{O}$ (green), $^{14}\text{N}^{18}\text{O}$ (orange) and $^{15}\text{N}^{18}\text{O}$ (indigo).